Research Article | Vol. 9, No. 6 | 1 Jun 2018 | BIOMEDICAL OPTICS EXPRESS 2810
Biomedical Optics EXPRESS

Biomimetic 3D-printed neurovascular phantoms for near-infrared fluorescence imaging

YI LIU,[1,2,4] PEJHMAN GHASSEMI,[2,4] ANDREW DEPKON,[2,3] MARIA IDA IACONO,[2] JONATHAN LIN,[2] GONZALO MENDOZA,[2] JIANTING WANG,[2] QINGGONG TANG,[1] YU CHEN,[1] AND T. JOSHUA PFEFER[2,*]

[1]*Department of Bioengineering, University of Maryland, Silver Spring, MD, USA*
[2]*Center for Devices and Radiological Health, U.S. Food and Drug Administration, Silver Spring, MD, USA*
[3]*Marquette University, Milwaukee, WI, USA*
[4]*Authors contributed equally to this work*
**Joshua.Pfefer@fda.hhs.gov*

Abstract: Emerging three-dimensional (3D) printing technology enables the fabrication of optically realistic and morphologically complex tissue-simulating phantoms for the development and evaluation of novel optical imaging products. In this study, we assess the potential to print image-defined neurovascular phantoms with patent channels for contrast-enhanced near-infrared fluorescence (NIRF) imaging. An anatomical map defined from clinical magnetic resonance imaging (MRI) was segmented and processed into files suitable for printing a forebrain vessel network in rectangular and curved-surface biomimetic phantoms. Methods for effectively cleaning samples with complex vasculature were determined. A final set of phantoms were imaged with a custom NIRF system at 785 nm excitation using two NIRF contrast agents. In addition to demonstrating the strong potential of 3D printing for creating highly realistic, patient-specific biophotonic phantoms, our work provides insight into optimal methods for accomplishing this goal and elucidates current limitations of this approach.

OCIS codes: (170.6280) Spectroscopy, fluorescence and luminescence; (180.1655) Coherence tomography.

References and links

1. T. J. Pfefer and A. Agrawal, "A review of consensus test methods for established medical imaging modalities and their implications for optical coherence tomography," Proc. SPIE **8215**, 82150D (2012).
2. M. A. Gavrielides, R. Zeng, L. M. Kinnard, K. J. Myers, and N. Petrick, "Information-theoretic approach for analyzing bias and variance in lung nodule size estimation with CT: a phantom study," IEEE Trans. Med. Imaging **29**(10), 1795–1807 (2010).
3. K. L. Lurie, G. T. Smith, S. A. Khan, J. C. Liao, and A. K. Ellerbee, "Three-dimensional, distendable bladder phantom for optical coherence tomography and white light cystoscopy," J. Biomed. Opt. **19**(3), 036009 (2014).
4. B. D. Killory, P. Nakaji, L. F. Gonzales, F. A. Ponce, S. D. Wait, and R. F. Spetzler, "Prospective evaluation of surgical microscope-integrated intraoperative near-infrared indocyanine green angiography during cerebral arteriovenous malformation surgery," Neurosurgery **65**(3), 456–462 (2009).
5. H. A. Zaidi, A. A. Abla, P. Nakaji, S. A. Chowdhry, F. C. Albuquerque, and R. F. Spetzler, "Indocyanine green angiography in the surgical management of cerebral arteriovenous malformations: lessons learned in 130 consecutive cases," Neurosurgery **10**(2), 246–251 (2014).
6. M. A. Kamp, S. Sarikaya-Seiwert, A. K. Petridis, T. Beez, J. F. Cornelius, H. J. Steiger, B. Turowski, and P. J. Slotty, "Intraoperative indocyanine green–based cortical perfusion assessment in patients suffering from severe traumatic brain injury," World Neurosurg. **101**(101), 431–443 (2017).
7. E. M. Sevick-Muraca, R. Sharma, J. C. Rasmussen, M. V. Marshall, J. A. Wendt, H. Q. Pham, E. Bonefas, J. P. Houston, L. Sampath, K. E. Adams, D. K. Blanchard, R. E. Fisher, S. B. Chiang, R. Elledge, and M. E. Mawad, "Imaging of lymph flow in breast cancer patients after microdose administration of a near-infrared fluorophore: feasibility study," Radiology **246**(3), 734–741 (2008).
8. C. M. Ho, A. Dhawan, R. D. Hughes, S. C. Lehec, J. Puppi, C. Philippeos, P. H. Lee, and R. R. Mitry, "Use of indocyanine green for functional assessment of human hepatocytes for transplantation," Asian J. Surg. **35**(1), 9–15 (2012).

#327661 https://doi.org/10.1364/BOE.9.002810
Journal © 2018 Received 6 Apr 2018; revised 17 May 2018; accepted 18 May 2018; published 29 May 2018

Biomedical Optics EXPRESS

9. D. S. Kittle, A. Mamelak, J. E. Parrish-Novak, S. Hansen, R. Patil, P. R. Gangalum, J. Ljubimova, K. L. Black, and P. Butte, "Fluorescence-guided tumor visualization using the tumor paint BLZ-100," Cureus **6**(9), e210 (2014).
10. V. O. Korhonen, T. S. Myllyla, M. Y. Kirillin, A. P. Popov, A. V. Bykov, A. V. Gorshkov, E. A. Sergeeva, M. Kinnunen, and V. Kiviniemi, "Light propagation in NIR spectroscopy of the human brain," IEEE J. Sel. Top. Quantum Electron. **20**(2), 289–298 (2014).
11. B. W. Pogue and M. S. Patterson, "Review of tissue simulating phantoms for optical spectroscopy, imaging and dosimetry," J. Biomed. Opt. **11**(4), 041102 (2006).
12. R. Long, T. King, T. Akl, M. N. Ericson, M. Wilson, G. L. Coté, and M. J. McShane, "Optofluidic phantom mimicking optical properties of porcine livers," Biomed. Opt. Express **2**(7), 1877–1892 (2011).
13. L. Luu, P. A. Roman, S. A. Mathews, and J. C. Ramella-Roman, "Microfluidics based phantoms of superficial vascular network," Biomed. Opt. Express **3**(6), 1350–1364 (2012).
14. J. Wang, J. Coburn, C. P. Liang, N. Woolsey, J. C. Ramella-Roman, Y. Chen, and T. J. Pfefer, "Three-dimensional printing of tissue phantoms for biophotonic imaging," Opt. Lett. **39**(10), 3010–3013 (2014).
15. A. Corcoran, G. Muyo, J. van Hemert, A. Gorman, and A. R. Harvey, "Application of a wide-field phantom eye for optical coherence tomography and reflectance imaging," J. Mod. Opt. **62**(21), 1828–1838 (2015).
16. B. Z. Bentz, A. V. Chavan, D. Lin, E. H. Tsai, and K. J. Webb, "Fabrication and application of heterogeneous printed mouse phantoms for whole animal optical imaging," Appl. Opt. **55**(2), 280–287 (2016).
17. L. A. Dempsey, M. Persad, S. Powell, D. Chitnis, and J. C. Hebden, "Geometrically complex 3D-printed phantoms for diffuse optical imaging," Biomed. Opt. Express **8**(3), 1754–1762 (2017).
18. E. Dong, Z. Zhao, M. Wang, Y. Xie, S. Li, P. Shao, L. Cheng, and R. X. Xu, "Three-dimensional fuse deposition modeling of tissue-simulating phantom for biomedical optical imaging," J. Biomed. Opt. **20**(12), 121311 (2015).
19. E. Maneas, W. Xia, D. I. Nikitichev, B. Daher, M. Manimaran, R. Y. J. Wong, C. W. Chang, B. Rahmani, C. Capelli, S. Schievano, G. Burriesci, S. Ourselin, A. L. David, M. C. Finlay, S. J. West, T. Vercauteren, and A. E. Desjardins, "Anatomically realistic ultrasound phantoms using gel wax with 3D printed moulds," Phys. Med. Biol. **63**(1), 015033 (2018).
20. S. J. Arconada-Alvarez, J. E. Lemaster, J. Wang, and J. V. Jokerst, "The development and characterization of a novel yet simple 3D printed tool to facilitate phantom imaging of photoacoustic contrast agents," Photoacoustics **5**, 17–24 (2017).
21. P. Diep, S. Pannem, J. Sweer, J. Lo, M. Snyder, G. Stueber, Y. Zhao, S. Tabassum, R. Istfan, J. Wu, S. Erramilli, and D. Roblyer, "Three-dimensional printed optical phantoms with customized absorption and scattering properties," Biomed. Opt. Express **6**(11), 4212–4220 (2015).
22. P. Ghassemi, J. Wang, A. J. Melchiorri, J. C. Ramella-Roman, S. A. Mathews, J. C. Coburn, B. S. Sorg, Y. Chen, and T. J. Pfefer, "Rapid prototyping of biomimetic vascular phantoms for hyperspectral reflectance imaging," J. Biomed. Opt. **20**(12), 121312 (2015).
23. P. Ghassemi, B. Wang, J. Wang, Q. Wang, Y. Chen, and T. Joshua Pfefer, "Evaluation of mobile phone performance for near-infrared fluorescence imaging," IEEE Trans. Biomed. Eng. **64**(7), 1650–1653 (2017).
24. M. I. Iacono, E. Neufeld, E. Akinnagbe, K. Bower, J. Wolf, I. Vogiatzis Oikonomidis, D. Sharma, B. Lloyd, B. J. Wilm, M. Wyss, K. P. Pruessmann, A. Jakab, N. Makris, E. D. Cohen, N. Kuster, W. Kainz, and L. M. Angelone, "MIDA: a multimodal imaging-based detailed anatomical model of the human head and neck," PLoS One **10**(4), e0124126 (2015).
25. T. M. Bücking, E. R. Hill, J. L. Robertson, E. Maneas, A. A. Plumb, and D. I. Nikitichev, "From medical imaging data to 3D printed anatomical models," PLoS One **12**(5), e0178540 (2017).
26. S. A. Prahl, M. J. C. van Gemert, and A. J. Welch, "Determining the optical properties of turbid mediaby using the adding-doubling method," Appl. Opt. **32**(4), 559–568 (1993).
27. W. Cheong, "Summary of Optical Properties," in *Optical-Thermal Response of Laser-Irradiated Tissue*, A. J. Welch and M. J. C. Van Gemert, Eds. (Plenum Press:, 1995)
28. P. van der Zee, M. Essenpreis, and D. T. Delpy, "Optical properties of brain tissue," Proc. SPIE **1888**, 454–465 (1993).
29. M. V. Marshall, J. C. Rasmussen, I. C. Tan, M. B. Aldrich, K. E. Adams, X. Wang, C. E. Fife, E. A. Maus, L. A. Smith, and E. M. Sevick-Muraca, "Near-infrared fluorescence imaging in humans with indocyanine green: a review and update," Open Surg. Oncol. J. **2**(2), 12–25 (2010).
30. A. Liebert, H. Wabnitz, H. Obrig, R. Erdmann, M. Möller, R. Macdonald, H. Rinneberg, A. Villringer, and J. Steinbrink, "Non-invasive detection of fluorescence from exogenous chromophores in the adult human brain," Neuroimage **31**(2), 600–608 (2006).
31. M. Kacprzak, A. Liebert, P. Sawosz, N. Żołek, D. Milej, and R. Maniewski, "Time-resolved imaging of fluorescent inclusions in optically turbid medium—phantom study," Opto-Electron. Rev. **18**(1), 37 (2010).
32. D. Milej, A. Gerega, N. Zołek, W. Weigl, M. Kacprzak, P. Sawosz, J. Mączewska, K. Fronczewska, E. Mayzner-Zawadzka, L. Królicki, R. Maniewski, and A. Liebert, "Time-resolved detection of fluorescent light during inflow of ICG to the brain-a methodological study," Phys. Med. Biol. **57**(20), 6725–6742 (2012).
33. S. C. Gebhart, W. C. Lin, and A. Mahadevan-Jansen, "In vitro determination of normal and neoplastic human brain tissue optical properties using inverse adding-doubling," Phys. Med. Biol. **51**(8), 2011–2027 (2006).
34. S. L. Jacques, "Optical properties of biological tissues: a review," Phys. Med. Biol. **58**(11), R37–R61 (2013).
35. J. Zhao, H. S. Ding, X. L. Hou, C. L. Zhou, and B. Chance, "*In vivo* determination of the optical properties of infant brain using frequency-domain near-infrared spectroscopy," J. Biomed. Opt. **10**(2), 024028 (2005).

Biomedical Optics EXPRESS

36. A. N. Yaroslavsky, P. C. Schulze, I. V. Yaroslavsky, R. Schober, F. Ulrich, and H. J. Schwarzmaier, "Optical properties of selected native and coagulated human brain tissues in vitro in the visible and near infrared spectral range," Phys. Med. Biol. **47**(12), 2059–2073 (2002).
37. A. Farina, A. Torricelli, I. Bargigia, L. Spinelli, R. Cubeddu, F. Foschum, M. Jäger, E. Simon, O. Fugger, A. Kienle, F. Martelli, P. Di Ninni, G. Zaccanti, D. Milej, P. Sawosz, M. Kacprzak, A. Liebert, and A. Pifferi, "In-vivo multilaboratory investigation of the optical properties of the human head," Biomed. Opt. Express **6**(7), 2609–2623 (2015).
38. C. A. Davies-Venn, B. Angermiller, N. Wilganowski, P. Ghosh, B. R. Harvey, G. Wu, S. Kwon, M. B. Aldrich, and E. M. Sevick-Muraca, "Albumin-binding domain conjugate for near-infrared fluorescence lymphatic imaging," Mol. Imaging Biol. **14**(3), 301–314 (2012).
39. L. Gagnon, A. F. Smith, D. A. Boas, A. Devor, T. W. Secomb, and S. Sakadžić, "Modeling of cerebral oxygen transport based on *in vivo* microscopic imaging of microvascular network structure, blood flow, and oxygenation," Front. Comput. Neurosci. **10**(82), 82 (2016).

1. Introduction

Performance standards for established medical imaging modalities commonly describe image quality test methods involving tissue-simulating phantoms with simplified internal and external geometries [1]. While such an approach is particularly useful for determining fundamental image quality characteristics (e.g., spatial resolution, low contrast detectability), biomimetic phantoms may also fill an important role in testing the performance of imaging systems. Realistic phantom geometries can enable more accurate task-based assessment of device essential performance [2] as well as software used to evaluate clinical images. Furthermore, such phantoms can help elucidate the effect of device design and biological variables under more clinically relevant conditions, thus potentially reducing the need for extensive animal and clinical testing. When used together, standard and biomimetic phantoms may provide complementary information that facilitates innovation and reduces the burden of regulatory testing while maintaining scientific rigor [3].

One area where biomimetic phantoms may be particularly useful is for evaluation of fluorescence-based surgical guidance systems. Near-infrared fluorescence (NIRF) imaging devices are commonly used with the passive contrast agent Indocyanine Green (ICG) for clinical cerebral angiography, including during surgeries for arteriovenous malformations and aneurisms [4–6]. This approach is also used to provide contrast-enhanced visualization for lymph node imaging [7] as well as cardiovascular and organ/tissue transplant surgeries [8]. Fluorescence molecular imaging approaches are also being developed to facilitate cerebral cancer surgery. To evaluate NIRF intraoperative brain imaging systems, a gelatin phantom with biomimetic surface geometry has been described, however, no vasculature or internal morphology was incorporated, and hydrogel phantoms are not sufficiently robust for long-term use [9]. Polymer-based phantoms [10] may be more well suited for performance evaluation of neurosurgical NIRF imaging products as well as for surgical training in procedures involving optical imaging.

In biophotonics, solid tissue-simulating phantoms have typically incorporated simple geometries such as layers, cylindrical channels and spherical inclusions, formed with basic molding techniques [11]. While molding has also been used to generate more complex structures [10], it is limited in its ability to generate complex, internal biomimetic features in a repeatable manner. Some groups have implemented techniques capable of producing more complex morphologies including photolithography for mimicking irregular vascular channels [12] – although this approach is limited to planar networks. Laser micromachining has also been used [13] for generating phantoms, however, the capability of these approaches is limited, and use represents a high degree of complexity and relatively high fabrication cost.

Three-dimensional (3D) printing represents a novel and rapidly evolving technology capable of fabricating polymer structures with arbitrary complexity in a highly repeatable manner. Several years ago, we pioneered the use of this approach for fabrication of turbid, tissue-simulating biophotonic phantoms [14] and provided preliminary images of linear channel phantoms with hyperspectral imaging and optical coherence tomography. Subsequently, additional studies have reported the development of 3D-printed phantoms for

Biomedical Optics EXPRESS

optical coherence tomography [15], diffuse optical tomography [16, 17], and hyperspectral reflectance imaging [18]. Other studies have used 3D-printing to generate molds for phantom fabrication, including photoacoustic imaging applications [19, 20]. A limited number of studies have also addressed customizing optical properties and printing heterogeneous phantoms with materials that mimic different tissue regions [16, 18, 21]. However, no prior studies have produced biomimetic phantoms with patent neurovasculature suitable for simulating clinical biophotonic imaging modalities such as contrast-enhanced NIRF.

Previously, we have fabricated 3D-printed phantoms incorporating morphology derived from human retinal vasculature, and imaged them with a hyperspectral reflectance oximetry system [22] and a NIRF imaging device using ICG contrast [23]. However, the vascular network used in these studies was semi-planar. Therefore, the purpose of this study was to provide a proof of principle for 3D printing of biomimetic optical phantoms defined with volumetric, patient-derived medical imaging data, with a focus on cerebral applications. In a broader sense, this work was also intended provide insights into 3D printing useful for non-optical applications in medicine and biology. Specific goals included identifying computer-based and experimental methods for fabrication and cleaning complex vascular phantoms with realistic optical properties, validating phantom morphology and performing NIR fluorescence imaging of biomimetic phantoms filled with commercially available contrast agents.

2. Methods

An overview of major steps in this project is provided in Fig. 1. To generate our phantom design, we used an MRI-defined anatomical model of the head which had been semi-automatically segmented and reconstructed in previous work by Iacono et al [24]. We edited and converted the file into a printable STL file format. The geometry was printed in biologically relevant polymers, then extensive cleaning of external surfaces and internal hollow channel regions was performed and NIR fluorescence images acquired with an ICG-blood mixture.

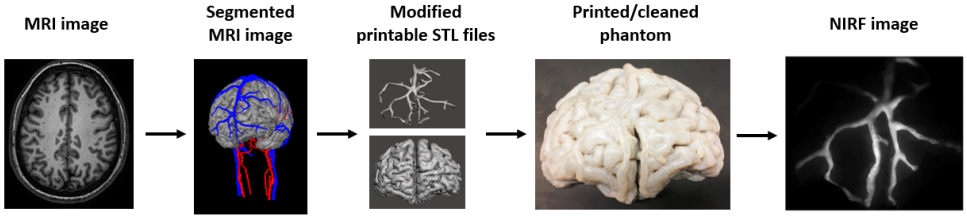

Fig. 1. Overview of process for generating biomimetic, image-defined neurovascular phantoms, leading to NIR fluorescence imaging. The segmented MRI-image-defined data volume was generated by Iacono *et al*. [24].

2.1 Volumetric digital map

In order to generate phantoms incorporating realistic brain morphology, we used a previously published MRI-defined volumetric model of the human head [24]. This model incorporates 15 segmented tissue types, including the four regions used in this study: gray matter, white matter, veins and arteries (Fig. 2). Magnetic resonance angiography sequences (MRA) (time of flight TOF and phase contrast PCA MRA) were acquired to enhance the visualization and segmentation of the arteries and the veins in the head. The TOF sequence encodes flow direction and was optimized to highlight blood flowing in cranial direction, which resulted mostly in arteries being visible. The PCA imaging was instead optimized to enhance imaging of slower flow vessels such as the veins and suppress the signal from the major fast flowing arteries.

Biomedical Optics EXPRESS

The maximum spatial resolution of the original MRI was 0.5 mm x 0.5 mm x 0.5 mm; thus, the segmentation was limited to the large vessels discernable on the images. A region of the segmented cerebral image volume in the frontal lobe (102 mm x 79 mm x 35 mm, Fig. 2(b)-(e)) was selected to help ensure that the fabrication approach was manageable. This region includes the prefrontal cortex and is supplied by polar and orbital frontal arteries; however, the primary vascular network in this region is the anterior portion of the superior sagittal sinus, with anterior frontal and frontopolar veins.

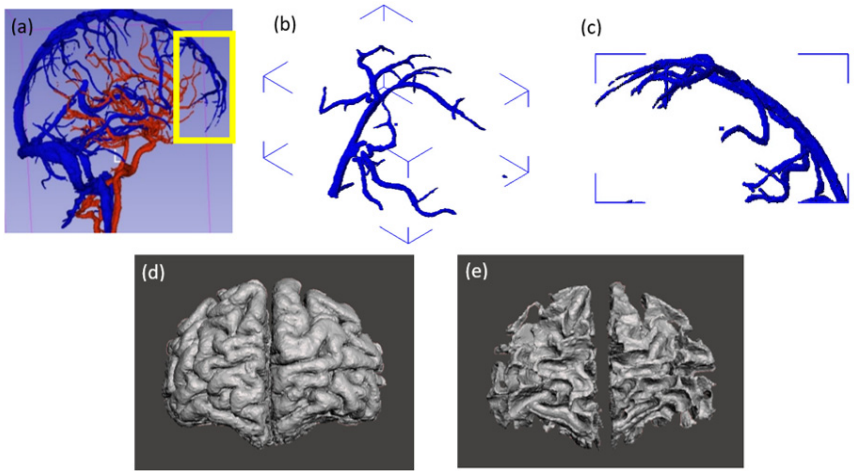

Fig. 2. Illustration of the main components of the digital neurovascular map generated from the MRI volumetric model [24]: (a) full network of larger arteries (red) and veins (blue), and frontal lobe region used in this study, including (b, c) vasculature, (d) grey matter, and (d) white matter.

Initial attempts to 3D-print and fill vascular phantoms with fluids indicated that some channels were not patent despite extensive cleaning. While nominal layer resolution and accuracy can be as low as 0.1 mm, we found that viable linear channels could be printed at diameters slightly less than 1 mm, irregular 3D networks required channels of about 1.5 mm diameter. Therefore, we used the software Autodesk Meshmixer (Autodesk, San Rafael, CA) to modify the original MRI-based vascular map with the software to increase the diameter of most vessels. Then, a combination Boolean method was used to combine the vein and artery maps. To ensure all vessels were connected to the superior sagittal sinus and open to the back of the phantom for injection, some vessels were connected, some lengthened and some inflated to an average of 1.7 mm diameter. After all these modification, the 3D model is smoothed and refined in Meshmixer [25]. An illustration of these design modifications is provided in Fig. 3(a).

Based on this vascular structure, we created two phantoms. The first was a homogeneous rectangular matrix (109 mm x 84 mm x 39 mm) with a 3D network of channels having 2.0 mm to 5.1 mm diameters (Fig. 3(a)). This was performed in part as a preliminary test of the ability to generate and clean a 3D vessel matrix. Given that all vasculature was contained within the homogeneous matrix, there was minimal potential for damage associated with printing and cleaning thin-walled superficial channels. Additionally, since the phantom had a flat surface, it could be more easily used for assessing imaging depth (Fig. 3(b)).

The second biomimetic phantom provided curved realistic surface and subsurface morphology, including white and grey matter regions in addition to the vascular network (Fig. 3(c),(d)). This phantom contained thin vessel walls which were difficult to print and clean (internally and externally) without extensive damage. To improve structural integrity, the curved phantom's superficial vessel walls were increased to a minimum thickness of 1.5 mm. Grey and white matter were printed simultaneously with two different materials.

Biomedical Optics EXPRESS

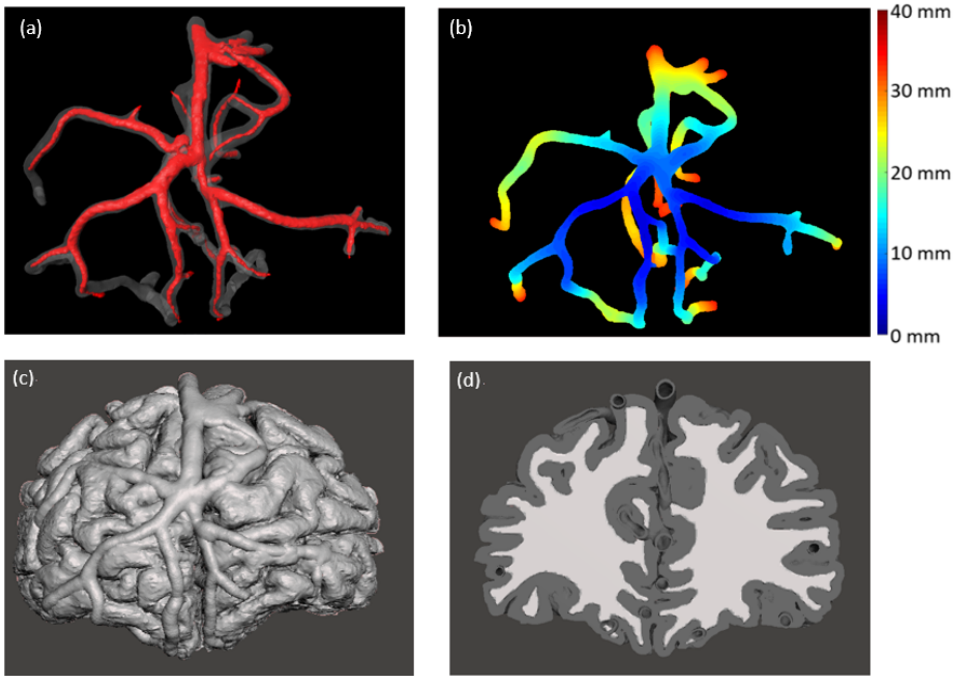

Fig. 3. Neurovascular phantom design. (a) Modified channels with enlarged diameters, (b) Color-coded illustration of channel depth in rectangular neurovascular phantom, unit is mm, (c) & (d) Design of morphologically-mimic neurovascular phantom, front view (c) and back view (d)

2.2 Printers and photopolymers

In this study, we used a commercial printer (Objet260 Connex3, Stratasys Inc., Eden Prairie, MN) for phantom fabrication. The printer is based on the "Polyjet" technique, in which UV light is used to cure droplets of liquid photopolymer from multiple heads that spray outlines of the printing part slice by slice. This technique has several advantages over other rapid prototyping techniques (such as Stereolithography and fused deposition modeling), including the ability to simultaneously print combinations of three different printing materials and high printing resolution (x- and y-axis: 600 dpi; z-axis: 1600 dpi). After testing several proprietary white materials available for use with this printer, we identified the one with the highest scattering coefficient (VeroWhite, Stratasys Inc., Eden Prairie, MN). This material was combined with a black material (TangoBlack, Stratasys Inc., Eden Prairie, MN) in different concentrations to generate samples with different absorption coefficients.

To measure optical properties of 3D printing materials, several 4 cm x 4 cm x 1 mm slabs were printed. Diffuse reflectance and transmittance were measured from 700 to 1000 nm using a dual-beam integrating sphere spectrophotometer (Lambda 1050, PerkinElmer Inc., Hopkinton, MA). Absorption and reduced scattering coefficients were calculated at each wavelength using the inverse adding-doubling method [26]. Optical properties are shown in Fig. 4 for a 100% white material, as well as a proprietary gray material (RGD-8510) created from a mixture of the aforementioned white and black materials. Both materials provided scattering coefficient levels in the 5-6 cm-1 range near 800 nm which is in moderately good agreement with cerebral optical properties from the literature [27, 28]. While the white material was used for the rectangular phantom, both white and gray materials were used to simulate corresponding brain matter regions of the curved-surface biomimetic phantom.

Biomedical Optics EXPRESS

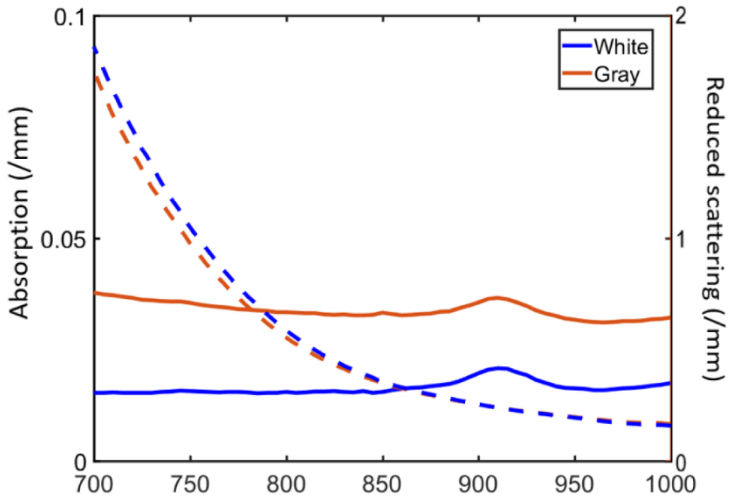

Fig. 4. Optical properties of combined 3D printing materials, including absorption and reduced scattering coefficients. Results are presented for a 100% white material as well as a mixture of white and black materials. (Absorption coefficient: Solid line; Reduced scattering coefficient: Dashed line)

2.3 Finishing process

After printing, it is necessary to remove the support materials used by the printer to maintain structural integrity of the sample during the polymerization process. These materials are designed to be readily removable and dissolvable. The cuboid phantom was cleaned by soaking in a 2% sodium hydroxide and 1% sodium metasilicate solution (WaterWorks, Stratasys, Eden Prairie, MN) while stirring the solution at a rate of 400 rpm for 2 days on the digital hotplate stirrer (SoCal BioMed, Newport Beach, CA). After that, the cleaning solution was pumped through a 25G needle into the channels for softening, dissolving and drawing out the supporting materials. For some channels, soft copper wires were applied for deeper cleaning of irregular channels. After all channels were assessed as being patent, the phantom was immersed in the cleaning solution for 1 day as a final step.

For the biomimetic phantom, support material surrounding printed parts was removed by rinsing under running water and gently rubbing the surface. Cleaning of the small, tortuous thin-walled channels of this phantom without causing damage was one of the most demanding aspects of the fabrication process. Identifying best practices involved extensive trial and error. While the proprietary solution was initially used to clean channels, this produced damage to the biomimetic phantom. Ultimately, we used a sonicating bath (Aquasonic 50D Ultrasonic Cleaner, VWR Scientific Products, Radnor, PA) for about 3 hours to loosen internal support material. This was performed in increments of 1 hour to avoid excessive heating. We then used a waterjet (Powerblast High Pressure Water Cleaner, Balco UK, Birmingham, UK) unit to eject support material from the channels. In the final biomimetic phantom, the cleaning process induced two small holes in superficial vessels which were subsequently sealed with clear epoxy.

2.4 Morphological validation

Preliminary evaluation of internal channel patency was performed with colored fluids. Imaging with microCT was then used as a final check to ensure that all support material had been removed, as well as to evaluate overall print quality. However, this was only possible with the biomimetic phantom, due to sample size limitations of the microCT system. To verify morphology, 1170 images were acquired with a resolution of 82 μm. Algorithms were executed in Matlab (TheMathWorks, Inc. Natick, MA) to process these images, reducing the

Biomedical Optics EXPRESS

shot noise of all the 2D images with a 3 x 3 median filter, converting into binary maps with an appropriate threshold and stacking into a 3D image volume. 3D visualization of the image volume was performed with Amira software (Thermal Fisher, Hillsboro, OR, USA). Matlab was used to identify flaws in printing and quantify various aspects of phantom morphology, such as channel diameter.

2.5 NIR fluorescence imaging

To demonstrate neurovascular phantom utility, we performed imaging with a custom NIRF imaging system. As illustrated in Fig. 5, the system used a 1W light emitting diode (LED) source with central wavelength at 785 nm and 10 nm bandwidth (RLTMDL-785-1W-5, driver: RLTMxL PSU-LED, Roithner Lasertechnik GmbH, Vienna, Austria) providing 35 mW/cm^2 irradiance at the phantom surface. An 800-nm short-pass excitation filter (84-729, Edmund Optics, Barrington, NJ, USA) was placed in front of the LED to eliminate crosstalk between the light source and detected signals. Fluorescence emitted from the phantom was imaged through an 825 nm long-pass emission filter (86-078, Edmund Optics, Barrington, NJ, USA). The filtered light was detected by a 16-bit monochrome CCD camera (1200 x 1600 pixels, Alta U2000, Apogee Imaging Systems, Roseville, CA, USA). Camera control and recording was performed using Micro-Manager software (version 1.4.20, Univ. of California San Francisco, CA, USA). Image analysis was performed using Matlab .

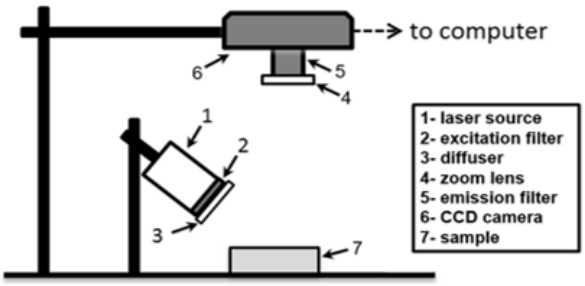

Fig. 5. Schematic illustrating layout of NIRF system(s).

Two different aqueous fluorescence solutions were prepared and injected into the channels of each phantom, separately: 1) ICG-bovine blood mixture with 3.2 µM of ICG (Pulsion Medical Inc., Powell, OH, USA), and 2) IR800-bovine blood mixture with 50 nM of IR800 (IRDye800 800CW Carboxylate, LI-COR, Lincoln, NE, USA) into the vascular channels of the brain phantom. In a previous *in vivo* animal study [29], the authors used 50 nM IR800 to quantify and assess IR800 performance. In clinics, the recommended dose for ICG angiography is 0.2 to 2 mg/kg with a maximum dose of 5 mg/kg/day [4]. Typically, ICG will be diluted to around 2.5 mg/ml for intravenous injection in humans [29]. In Liebert's study [30], researchers injected 11mg ICG diluted in 3 ml of saline intravenously into volunteers and measured the concentration of ICG in brain tissue to be about 1.7 µM. Other groups have used a minimum of 2.5 µM ICG for turbid phantom fabrication [31], and 0.08 µM to 1.03 µM in a blood vessel model [32]. Therefore, to better test the performance of our neurovascular phantoms, 50 nM IR800 and 3.2 µM ICG were chosen in our study. These solutions were then formulated with fresh defibrinated bovine blood (Quad Five, Ryegate, MT, USA). The filled phantom was then placed in a vacuum chamber for degassing for about 5 minutes, after which all the phantom openings on the bottom were sealed using hard glue.

Biomedical Optics EXPRESS

3. Results

3.1 Printed phantoms

Significant challenges were encountered in fabricating biomimetic phantoms with viable vasculature. As noted in some of small channels often experienced cracks in the vessel walls (e.g., Fig. 6(a)) due to the use of a high pressure microjet. While revised methods to minimize such damage were highly effective, additional leaks in the phantom were still noted. To identify the source of these leaks, microCT imaging was performed. We acquired a stack of 1170 microCT images of two early biomimetic phantoms, from which a digital model was reconstructed. This model was used to visualize surface and subsurface regions, including vasculature. The attached movie illustrates a flythrough of these images for two phantoms imaged with microCT (see Visualization 1). Two images extracted from this data set are shown in Fig. 6(b),(c). These images illustrate regions of the phantom where cracks occurred on internal portions of superficial vessels that were not apparent through inspection of the phantom surface. These types of imperfections were addressed by increasing vessel wall thickness in specific locations.

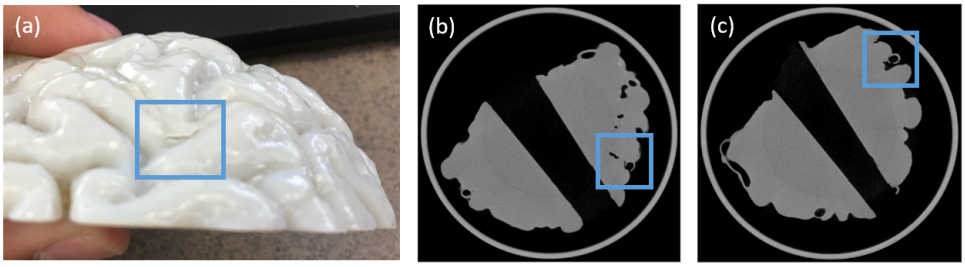

Fig. 6. Flaws in 3D-printed curved-surface neurovascular phantom, including: (a) an external crack on the surface of the phantom; (b) the same external crack visualized with microCT imaging; and (c) an internal crack in a subsurface area which was not readily apparent on inspection but clearly seen with microCT.

Fabrication and cleaning of the rectangular neurovascular phantom were less challenging because all channels were surrounded by solid material, and at least 4 mm below the phantom surface. However, after this phantom was printed and cleaned, initial NIRF imaging indicated that a section of the vasculature was blocked. Since the large size of the phantom precluded microCT imaging, we used a thin, flexible wire to loosen a section of support material that was blocking a channel. When the final phantom was injected with solutions containing blood, superficial veins were apparent under visible light illumination (Fig. 7(a)). Due to high turbidity, internal arteries could not be readily visualized.

Photographs of final rectangular and biomimetic phantoms are shown in Fig. 7. When the rectangular phantom was filled with blood solutions, superficial veins within 4 mm of the surface were visible under visible light illumination. Deeper internal arteries could not be readily visualized due to high phantom turbidity. The biomimetic phantom shown in Fig. 7(b),(c) exhibits blood-filled surface vasculature. While most vessels run along the surface of the gray matter, several segments were seen penetrating the tissue surface. From the back view of the phantom, the irregular border between white and gray matter regions is clearly distinguishable, as are the larger vessels used to inject blood-ICG solutions. Final biomimetic phantom microCT images were acquired for qualitative and quantitative validation of printing accuracy.

Biomedical Optics EXPRESS

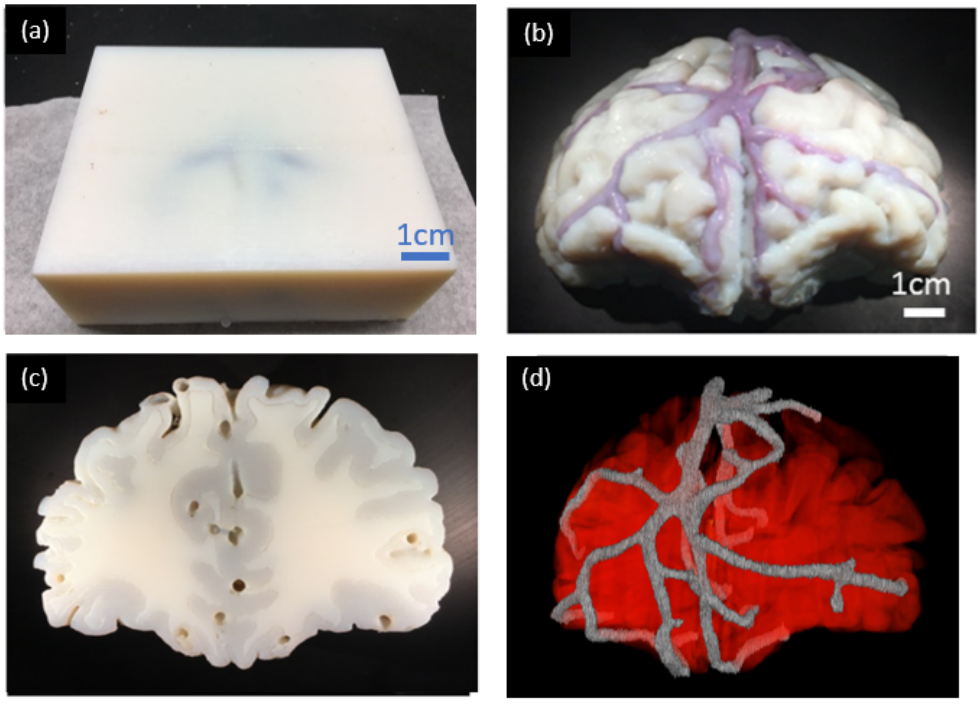

Fig. 7. (a) 3D-printed rectangular neurovascular phantom and (b) 3D-printed morphologically-mimic neurovascular phantom, Channels are filled with blood-ICG solution. (c) Back view of the morphologically-mimic neurovascular phantom, (d) Reconstructed microCT image of neurovascular phantom.

Using a custom Matlab routine, the morphology of the final biomimetic phantom was compared with the original MRI image volume and nominal phantom design. Inner diameters of vessels at 22 representative locations are measured and compared, these locations including arteries and veins, superficial and deep area, are shown in Fig. 8(a),(b). The magnitude of increase in vessel lumen diameter from the original MRI image volume to final phantom is shown in Fig. 8(c). The mean enlargement in lumen diameter is 66.8%. The comparison of the diameter of vessels in printed phantom and its corresponding digital design is shown Fig. 8(d), we found that most channels were printed smaller than its design and the overall deviation is 6%. There are two major reasons for this deviation: the resolution of the printer for channel printing and our post-printing cleaning method that there could still exist some supporting materials in the channels not thoroughly cleaned.

Biomedical Optics EXPRESS

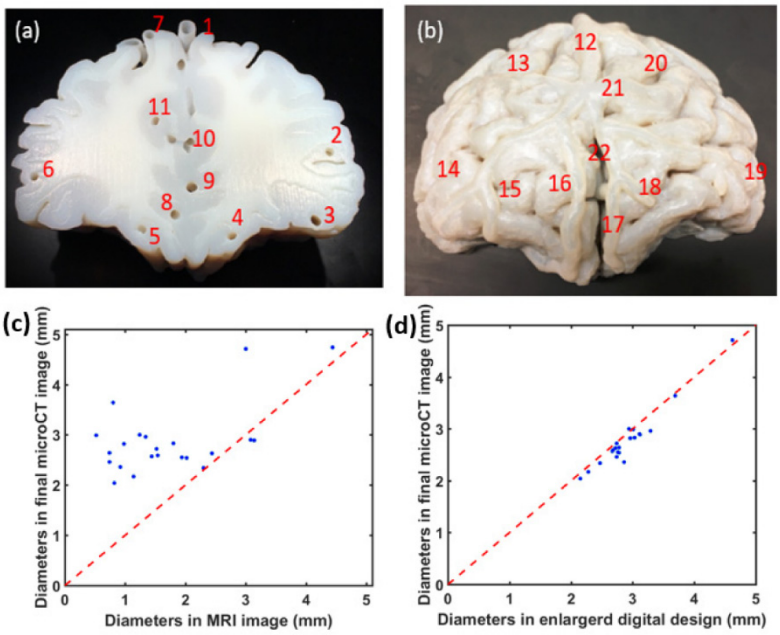

Fig. 8. (a)&(b) 22 typical locations of channels chosen for quantification of the channel sizes. (c) Comparison of vessel diameters between MRI image volume and final printed phantom; (d) vessel diameters in enlarged digital design and final printed phantom. Blue dots referred to different locations shown in (a)&(b).

3.2 Near-infrared fluorescence imaging

We used a custom NIRF system to image the rectangular phantoms injected with solutions of bovine blood and ICG or IR800 (Fig. 9). By correlating these results with the map of vessel depth distributions shown in Fig. 3(b), we determined that imaging depths of up to 12 mm were achieved. The ICG image shows bright signal level and relatively little noise. However, a diffuse fluorescent light is seen surrounding the vascular network. Additionally, the distant vessels become increasingly blurry as they increase with depth, due to phantom turbidity. Results for IR800 show the ability to resolve a similar extent of vasculature, as well as similar depth-dependent light diffusion effects. We determined the signal to noise ratio (SNR) for 10 approximately identical vessel locations in both images of Fig. 9. Based on data in Fig. 3(b), the vessels at these locations had depths of 3.1 to 8.5 mm. Results indicated both strong correlations in SNR with depth and contrast agent, specifically values of 17.8 to 3.6 for ICG and 10.3 to 1.7 for IR800. The lower SNR values for IR800 were likely due primarily to the low agent concentration used (50 nM, vs. 3.2 μM for ICG),

Biomedical Optics EXPRESS

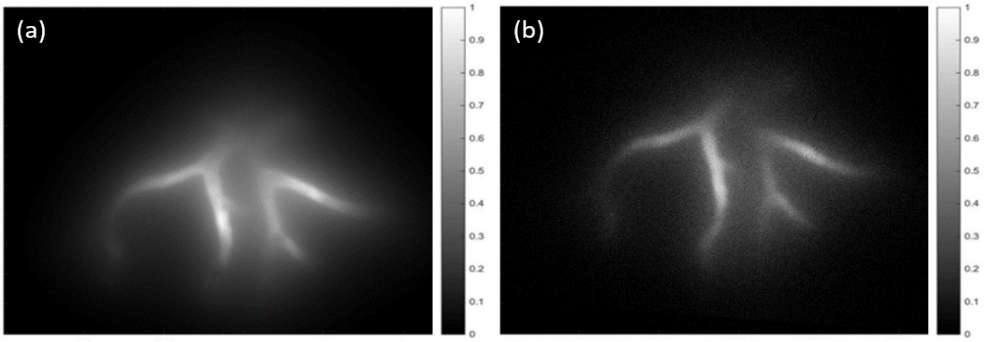

Fig. 9. NIRF images of rectangular neurovascular phantom in Fig. 7(a) filled with (a) ICG and (b) IR800.

We imaged the curved-surface biomimetic neurovascular phantom with the same system and fluorophore solutions as the rectangular phantom. Results (Fig. 10(a),(d)) show well-defined, high-contrast vessels without the diffusion effect seen for subsurface vessels in the rectangular phantom. However, some variability in signal intensity along the channels is apparent. The white light images illustrate highly realistic brain surface morphology, including numerous cerebral sulci and superficial vasculature appearing as darker regions with low contrast. The combined white light and NIR fluorescence overlay images are seen in Fig. 10(c),(f). These images strongly highlight the vasculature against cerebral tissue structures, illustrating the utility of fluorescence imaging for intraoperative visualization and providing results with strong visual similarity to clinical images [5]. However, these images also show significant non-uniformity in NIRF signal intensity from the center of the image. Quantitative evaluation of SNR in corresponding high-contrast superficial vessel locations produced values of 158 for ICG versus 81 for IR800.

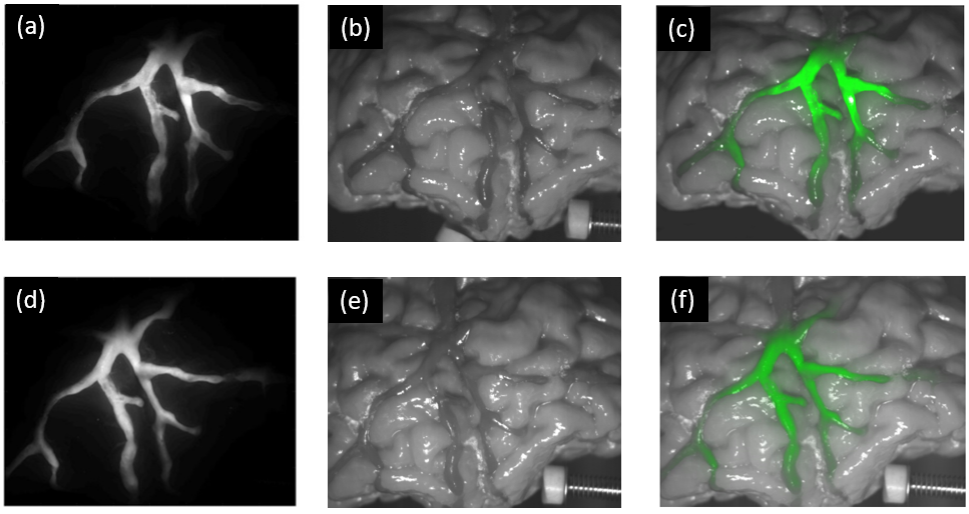

Fig. 10. NIRF (a,d), white light (b,e) and combined overlay images (c, f) of the biomimetic neurovascular phantom filled with ICG (a, b, c) and IR800 (d, e, f).

4. Discussion

Morphologically and optically realistic tissue-simulating phantoms represent powerful tools for development, evaluation, and translation of biophotonic technology. The cerebral phantoms presented here demonstrate the first successful fabrication of 3D vascularized models for biophotonic imaging defined from a human subject image volume. The

Biomedical Optics EXPRESS

biomimetic phantom in Fig. 10 produces white light and NIRF images that appear strikingly realistic, particularly in comparison to prior cerebral phantoms for biophotonics [10, 17]. We have also presented a rectangular phantom incorporating biomimetic vasculature that is particularly well suited to quantitative testing of penetration depth. By incorporating complex neurovascular morphology and implementing fluorophores relevant to current clinical practices as well as emerging molecular imaging techniques, we have illustrated the potential of novel 3D printing techniques. In addition to providing this proof of concept, we have described practical methods that can be used to fabricate and rigorously validate similar phantoms for a wide range of applications.

4.1 Fabrication of biomimetic phantoms with 3D printing

The steps required before and after the actual 3D printing process include a range of challenges: segmenting an image volume into an accurate and effective digital model; identifying best practices for preprocessing and optimizing the digital model to best achieve ones goals given the limitations (e.g., resolution) of both the imaging modality (e.g., MRI) and the 3D printer; characterizing and selecting optically suitable materials; identifying best practices for support material removal and phantom cleaning (especially for phantoms involving small, tortuous channels), as well as identifying/correcting build imperfections and characterizing the morphology of the final phantom. While we have described approaches for addressing these challenges, the optimal solutions will vary based on the imaging system, printer, geometry and specific goals.

Selecting a 3D printer typically involves evaluating trade-offs in functionality and performance. In this study, we used a relatively expensive commercial 3D printer Objet 260 (approximately $250,000) for phantom fabrication. The total material cost for fabrication of a single phantom is about $75. Compared to most desktop fused filament fabrication (FDM) and stereolithography (SLA) 3D printers, Objet 260 can provide higher and is able to print three different materials simultaneously. Additionally, this printer can generate models that simulate heterogeneous, multi-component tissues, and generate both realistic surface and subsurface morphology, including vasculature, sulci and gyri. However, the optical property tuning capability was limited. The stock material used to simulate brain matter provided a scattering coefficient in the near-infrared that was biologically relevant. We were unable to identify a proprietary material with higher scattering, which might match the values suggested by some studies [28, 33–37] – particularly for white matter – although the literature indicates a lack of consensus on this value. Given that our imaging of primarily superficial cerebral vasculature requires more realism in gray matter than the deeper white matter, the selected materials were sufficient for this proof of principle. In the future, an ideal 3D printer for tissue phantom fabrication would provide both high resolution and the ability to simultaneously print multiple customized materials doped with absorbers and scatters.

In spite of our success in fabricating patient-specific neurovascular phantoms, several limitations remain. First, medical imaging systems capable of deep human tissue imaging, such as MRI, are not able to provide accurate geometries of vessels below 1 mm in diameter. Secondly, 3D printers have limited resolution for printing hollow channels, particularly in irregular 3D networks. Although nominal printing resolution values on the order of tens or hundreds of microns are often advertised, in our experience most printers are not able to reliably print patent linear channels smaller than 0.5 mm in diameter, or complex 3D networks with channels smaller than 1 mm diameter. Furthermore, even if printers were able to generate such channels, cleaning 3D printer support material from small-diameter and long, tortuous vessel segments can be difficult, and lead to damage in thin vessel walls. Therefore, to successfully fabricate a neurovascular phantom, we increased vascular lumen diameters from a mean of 1.72mm to 2.87 mm (66.8%), and wall thickness was increased by 1.5 mm, on average.

Biomedical Optics EXPRESS

MicroCT imaging proved a crucial tool for detecting and locating imperfections in printed and cleaned phantoms – such as blockages and vessel wall breaks – as well as for performing quantitative evaluations of build quality. This information was used to revise digital models, evaluate channel cleaning methods and realize a viable final product. Volumetric data sets acquired with microCT elucidated the limitations of our 3D printer. Additionally, our experience with this approach provided strong evidence of the need for rigorous quality control in complex models prior to implementation. However, other imaging approaches may be suitable as well. In a recent study, X-ray imaging was used to evaluate a 3D-printed full-size human head phantom [17]. This approach may be useful for phantoms that exceed the sample size limitations of microCT systems.

4.2 Contrast-enhanced fluorescence imaging

One of the primary benefits of biomimetic phantoms are their ability to act as medical device research and development tools for evaluating the optical instrumentation, contrast agents and software components of emerging technology. Images acquired in this study provide insights into the performance of our imaging system and two common fluorescence contrast agents. While previous *in vitro* studies have indicated that IR800 provides better results than ICG due to a higher extinction coefficient and quantum efficiency compared with ICG [29], the concentration of IR800 used in our study was much lower (50 nM) than ICG (3.2 μM); therefore, SNR values for ICG images were relatively higher than IR800. The images also illustrated NIRF imaging system non-uniformity, with portions of the vasculature near the center of the image showing much stronger signals than those near the edge. Furthermore, the same vessels appear to emit different levels of fluorescence in different images. This may be due to variations in angle and position of the target relative to the light source and camera, or local photobleaching of ICG. Penetration depth results from the rectangular phantom indicated that both fluorophores provided visualization of vasculature to a depth of approximately 12 mm. The fact that this falls short of the 2 to 4 cm imaging depths achieved in prior studies is likely due to the basic design of our system and modest camera sensitivity [38].

Our phantom measurements provide preliminary insights into performance testing capabilities; however, a wide variety of other novel testing approaches may be implemented in the future. Unlike the simple phantom designs used to determine fundamental image quality metrics, realistic phantoms enable objective and/or subjective testing under realistic clinical conditions. Advanced testing based on true clinical diagnostic tasks involving pathology-simulating phantoms may enable more effective product evaluations than ever before – such as the ability to accurate estimate changes in tumor volume [2]. For neurosurgery applications, it should be possible to implement structural pathologies such as AVMs and aneurysms, whereas inclusions representing diverse tumors morphologies and metastases could be incorporated for evaluating surgical oncology products based on molecular imaging. Alternately, such realistic models may be useful for facilitating surgical training on novel biophotonic products or for validating the simulation of complex light-tissue interactions in 3D computational models using patient-specific tissue morphology [39].

5. Conclusion

We have successfully developed 3D biomimetic neurovascular phantoms derived from the frontal lobe region of a clinical MRI image volume and performed NIRF imaging using two common fluorescent dyes. It was possible to visualize vasculature on surface areas of biomimetic phantom and subsurface areas of rectangular phantom. While additional improvements to increase the biological relevance of the phantoms are warranted, this work provides ample demonstration of the potential of 3D-printed biomimetic phantoms to enable performance assessment of bioimaging modalities under more realistic conditions than previously possible.

Biomedical Optics EXPRESS

Disclaimer

The mention of commercial products, their sources, or their use in connection with material reported herein is not to be construed as either an actual or implied endorsement of such products by the Department of Health and Human Services.

Funding

U.S. Food and Drug Administration (FDA) Critical Path Initiative, FDA's Medical Countermeasures Initiative; the National Science Foundation's FDA Scholar-in-Residence Award (CBET-1641077); ORISE fellowship program through Oak Ridge Associated Universities.

Acknowledgments

The authors gratefully acknowledge assistance provided by FDA's Additive Manufacturing of Medical Products (AMMP) Lab, supported by the Office of the Chief Scientist's Shared Resources program.

Disclosures

The authors declare that there are no conflicts of interest related to this article.